RSC Advances

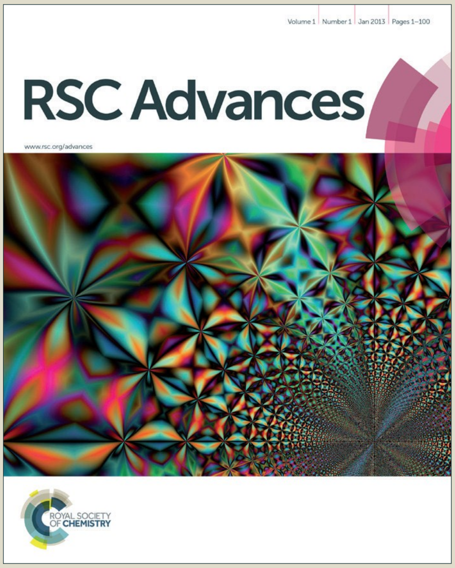

This is an *Accepted Manuscript*, which has been through the Royal Society of Chemistry peer review process and has been accepted for publication.

Accepted Manuscripts are published online shortly after acceptance, before technical editing, formatting and proof reading. Using this free service, authors can make their results available to the community, in citable form, before we publish the edited article. This *Accepted Manuscript* will be replaced by the edited, formatted and paginated article as soon as this is available.

You can find more information about *Accepted Manuscripts* in the Information for Authors.

Please note that technical editing may introduce minor changes to the text and/or graphics, which may alter content. The journal's standard Terms & Conditions and the Ethical guidelines still apply. In no event shall the Royal Society of Chemistry be held responsible for any errors or omissions in this *Accepted Manuscript* or any consequences arising from the use of any information it contains.

ROYAL SOCIETY
OF CHEMISTRY

www.rsc.org/advances

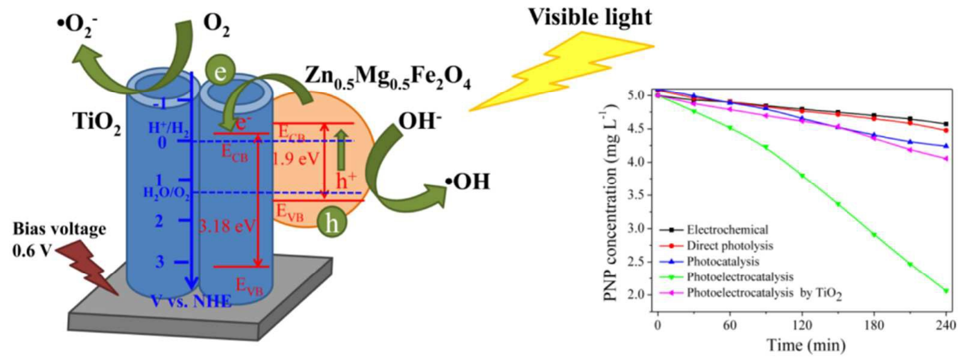

$Zn_{0.5}Mg_{0.5}Fe_2O_4$ nanoparticles contribute to widening the spectral response range and reducing the charge recombination of TiO_2 nanotube arrays.

RSC Advances Accepted Manuscript

Journal Name

ARTICLE

Synthesis of Novel $Zn_{0.5}Mg_{0.5}Fe_2O_4$@TiO_2 Nanotube Arrays with Enhanced Photoelectrocatalytic Properties

Received 00th January 20xx,
Accepted 00th January 20xx

DOI: 10.1039/x0xx00000x

www.rsc.org/

Jingqiang Pan[a], Xinyong Li[a,b,]*, Qidong Zhao[a], and Dongke Zhang*[b]

A novel nanocomposite electrode with tight and vertically aligned $Zn_{0.5}Mg_{0.5}Fe_2O_4$@TiO_2 nanotube arrays (NTs) has been successfully synthesized via an ultrasonically assisted electrodeposition strategy. The scanning electron microscopy (SEM), transmission electron microscopy (TEM) and X-ray diffraction (XRD) of the composite nanostructures indicated that the as-prepared electrodes were well-aligned TiO_2 NTs with $Zn_{0.5}Mg_{0.5}Fe_2O_4$ nanoparticles. The enhanced absorption of the nanocomposite electrode under simulated sun light and visible light regions were observed. The photoelectrochemical performance of $Zn_{0.5}Mg_{0.5}Fe_2O_4$@TiO_2 nanotube arrays showed excellent sensitive response to the visible light. The surface-interface charge separation and transfer of photo-induced electrons and holes were also demonstrated by optical characterization. Meanwhile, the photoelectrochemical investigations clearly illustrated that the $Zn_{0.5}Mg_{0.5}Fe_2O_4$@TiO_2 composite NTs had more effective photo-conversion capability than the unloaded TiO_2 NTs. The saturated photocurrent density of doped electrode was about 6.5 folds and 4 folds as high as that of the TiO_2 NTs under the illumination of visible light and simulated sun light, respectively. In addition, the enhanced photoelectrocatalytic (PEC) ability of the as-prepared electrode was demonstrated in the degradation of toxic p-nitrophenol species. The much improved PEC activity can be attributed to both the visible-light photocatalytic activity of $Zn_{0.5}Mg_{0.5}Fe_2O_4$ and the heterostructure between $Zn_{0.5}Mg_{0.5}Fe_2O_4$ and TiO_2.

Introduction

Semiconductor-based photocatalysts have received considerable attention due to their potential in environmental pollution remediation and renewable energy applications [1, 2]. TiO_2 nanostructure has in particular attracted tremendous interest due to its favourable photocatalytic (PC) activity, stability, anti-photocorrosion and non-toxicity [3-5]. Among various nanostructures, well aligned TiO_2 nanotube arrays (NTs) are especially interesting and intriguing because of their large surface area and short diffusion length perpendicular to the charge collecting substrate, leading to lower recombination loss, As such, TiO_2 NTs have been developed for a range of applications including photocatalysis [6-8], water splitting for hydrogen production [9], solar energy conversion [10, 11], lithium ion batteries [12] and gas sensors [13].

However, TiO_2 is a semiconductor with wide band gap (3.0 and 3.18 eV for the rutile and anatase, respectively) only functioning under UV light irradiation (just about 4.5% of solar energy). Therefore, development of visible light driven photocatalysts based on TiO_2 NTs becomes a key challenge but holds a key to widespread applications of this type of photocatalysts. Various strategies have been used to extend the absorption band of TiO_2 to the visible light region such as metal ion doping [14-17], nonmetal ion doping [18-20] and narrow-band-gap semiconductor composites [21-25]. The fact that the photon-generated electrons from the conduction band of the narrow band gap semiconductor could be injected into the conduction band of TiO_2 has been demonstrated, which not only can expand the spectral range of light absorption, but may also promote photon-excited electron-hole separation [17,18].

Recently, spinel ferrite ($MeFe_2O_4$, where Me usually represents a metal,such as Zn, Mg, Mn, Ni etc.) crystallites are considered good candidate for photocatalysis reaction in which Me^{2+} cations occupy tetrahedral sites [26, 27]. Spinel ferrites offer the advantage of having a band gap capable of absorbing visible light, as well as the spinel crystal structure providing available extra catalytic sites by the virtue of crystal lattice [28]. A great deal of work has been reported about the combination of spinel ferrites with TiO_2 to enhance the PC activity. Especially, $Zn_{0.5}Mg_{0.5}Fe_2O_4$ with a spinel structure has been recently investigated due to its chemical stability and sensitivity to visible light [29-31]. Rekha Dom has synthesized $Zn_{0.5}Mg_{0.5}Fe_2O_4$ via microwave irradiation [28], while S. Rahman has prepared ZnMg-ferrite nanoparticles using the co-precipitation method [32]. Besides, both the conduction band and the valence band of $Zn_{0.5}Mg_{0.5}Fe_2O_4$ locate at higher wavelengths than those of TiO_2, resulting in an excellent separation of the electron-hole pairs [27]. Furthermore, the spinel ferrite properties of the dopants can enhance the separation efficiency of the photon-generated charges as well as their reactivity

---

[a] Key Laboratory of Industrial Ecology and Environmental Engineering (MOE), State Key Laboratory of Fine Chemicals, School of Environmental Science and Technology, Dalian University of Technology, Dalian 116024, China.
[b] Centre for Energy (M473), The University of Western Australia, 35 Stirling Highway, Crawley, WA 6009, Australia.

† Footnotes relating to the title and/or authors should appear here.
Electronic Supplementary Information (ESI) available: [details of any supplementary information available should be included here]. See DOI: 10.1039/x0xx00000x

RSC Advances Accepted Manuscript

This journal is © The Royal Society of Chemistry 20xx

Please do not adjust margins

due to their internal electrostatic field [27, 33]. Consequently, coupling TiO_2 NTs with $Zn_{0.5}Mg_{0.5}Fe_2O_4$ nanoparticles seems a promising approach to enhancing visible light absorption due to the special semiconductor structure and spatial crystal spinel structure of the $Zn_{0.5}Mg_{0.5}Fe_2O_4$ ferrites.

In this current work, we have synthesized visible-light-responsive $Zn_{0.5}Mg_{0.5}Fe_2O_4$ coupled TiO_2 NTs via an ultrasonically assisted electrodeposition strategy. The properties of the heterojunction between the $Zn_{0.5}Mg_{0.5}Fe_2O_4$ and TiO_2 NTs electrode and the photoelectrochemical properties of $Zn_{0.5}Mg_{0.5}Fe_2O_4$@TiO_2 NTs electrode were determined and investigated using the photoelectrochemical techniques. In addition, the photoelectrocatalytic (PEC) activity of the electrodes was evaluated in detail by using the PEC degradation of toxic p-nitrophenol (PNP) species under simulated sun light and visible light irradiation conditions.

Experimental

Synthesis of $Zn_{0.5}Mg_{0.5}Fe_2O_4$@TiO_2 composite electrode

Titanium foil (purity 99.6%, thickness 0.2 mm) was acquired from Beijing Academy of Steel Service, China. All the other chemicals were of analytical grade. The titanium foil was mechanically polished with sand papers of different grade (fineness) and then rinsed clean in an ultrasonic bath of deionized water for 10 min. The clean, polished titanium foil was subjected to chemically etching by immersing it in a mixture of HF and HNO_3 ($HF/HNO_3/H_2O$ = 1:4:5 in volume) for 40s. The titanium foil was rinsed again in deionized water to remove the mixed acid, followed by final cleaning by immersing it in an ethanol and deionized water solution in the ultrasonic bath for 15 min. The anodization was performed in a two-electrode cell with titanium foil as the working electrode and platinum foil as the counter electrode. The anodizing voltage was set at 20 V and anodized for 30 min in 0.2wt% HF solution. After anodization, the sample was immediately rinsed with deionized water and dried at room temperature. The sample was then annealed at 773K in air for 2 h with heating and cooling rates of 2 °C/min to convert the amorphous phase to crystalline phase.

The deposition procedure was conducted in a three-electrode setup in an uniform cell, using the TiO_2 nanotube arrays electrode as the working electrode, a Pt foil as the counter electrode, and a saturated calomel electrode (SCE) as the reference electrode. The electrodeposition was carried out with a potential of –2.4 V for 20 min. Before electrodeposition, the sample was immersed in a mixture solution 50 mL containing 0.025 M (0.7425 g) $Zn(NO_3)_2{\cdot}6H_2O$, 0.025M (0.641 g) $Mg(NO_3)_2{\cdot}6H_2O$ and 0.1 M (4.04 g) $Fe(NO_3)_3{\cdot}9H_2O$ for 20 min in an ultrasonic bath at 40 kHz frequency, which drove the salt solution to diffuse through the nanochannels of TiO_2 and ensure that the inner walls of the pore channels were filled with the solution. Then the TiO_2 NTs electrode was diverted into a new medium that contained the supporting electrolyte (0.1 M Na_2SO_4, 80 mL). The deposition in this medium resulted in the deposition of Zn, Mg and Fe ions. After repeating the ultrasonication and deposition procedure several times, a desired amount of Zn, Mg and Fe deposition in the pores was achieved. Subsequently, the electrode was electrochemically oxidized in a 1 M KOH (70 mL) solution with a constant potential of 2.5 V for 5 min. Finally, the sample was rinsed with deionized water and dried in air. Then it was annealed by heating at 773K for 2 h at muffle furnace, with a ramp of 2 °C/min.

Characterization

The morphology of the $Zn_{0.5}Mg_{0.5}Fe_2O_4$@TiO_2 NTs was characterized using a field emission scanning electron microscope (SEM) (Quanta 450) with an accelerating voltage of 30.0 kV. The dopant concentration was characterized by energy-dispersive X-ray spectra (EDX) (Horiba 7593H), and EDX was performed to determine the elemental concentration distribution on the catalyst granules using Link Isis Series 300 software. Transmission electron microscopy (TEM) and high-resolution transmission electron microscopy (HRTEM) images were taken on a FEI Tecnai G^2 F20 with an acceleration voltage of 200 and 300 kV. Chloroform solutions containing these nanocomposite samples were dropped on carbon-coated copper grids. The crystallinity of the sample was determined from X-ray diffraction patterns (XRD) using a diffractometer with Cu Ka radiation (Shimadzu Lab-X XRD-6000, source light at the wavelength (λ) of 0.15406 nm). The accelerating voltage and applied current were 30 kV and 30 mA, respectively. while the diffraction angles (2θ) was scanned from 20° to 60°. The absorption property was measured using UV-Vis diffuse reflectance spectra (DRS) (JASCO, UV-550) with a wavelength range of 200-700 nm. Photoluminescence (PL) spectra of the electrode surface was collected using a Hitachi F-4500 (excited at λ = 325 nm) fluorescence spectrophotometer in air at room temperature. X-ray photoelectron spectroscope (XPS) (PHI 5600 mode) was performed to examine the surface properties and composition of the sample. All the binding energies were calibrated by using the carbon (C 1s) 284.6 eV as a reference. The separation characteristics of photon-generated charge carriers was tested using a surface photovaltage (SPV) measurement system, which consisted of a monochromator (model Omni-λ 3005) and a lock-in amplifier (model SR830-DSP) with an optical chopper (model SR540) running at a frequency of 20 Hz.

PEC activity measurement

Photoelectrochemical measurement

Photocurrent density was measured using a CHI electrochemical analyzer (CHI 760C, Shanghai Chenhua, China) in a standard three-electrode configuration with $Zn_{0.5}Mg_{0.5}Fe_2O_4$@TiO_2 NTs as the photoanode (an effective area of 5 cm^2), a platinum foil as the counter electrode, and a saturated calomel electrode (SCE) as the reference electrode. A 0.01 M Na_2SO_4 (80 mL) solution was used as the electrolyte. The working electrode was irradiated with visible light (λ > 420 nm) through a UV-cutoff filter (Shanghai Seagull Colored Optical Glass Co. Ltd.) from a high-pressure xenon short arc lamp (a Phillips 500 W Xe lamp). The incident light intensity was measured with a radiometer (Photoelectric Instrument Factory Beijing Normal University, model FZ-A).

Photoelectrochemical experiment

The PEC reactions of PNP were carried out in a single photoelectrochemical compartment. The corresponding

RSC Advances Accepted Manuscript

This journal is © The Royal Society of Chemistry 20xx

concentration of PNP species was obtained from diluting an analytical grade powder of PNP with deionized water. The as-prepared electrode serving as the photoanode and Pt foil as the cathode were placed in parallel in a cylindrical quartz reactor, and an SCE served as the reference electrode. All electrodes were connected to a CHI 760C EC analyzer. A bias potential applied on the photoanode was 0.6 V (vs SCE) under visible light of 33.5 mW cm^{-2} and simulated sun light of 36 mW cm^{-2}, respectively. All the experiments were performed with magnetic stirring, using a 0.01 M Na_2SO_4 solution as the electrolyte. The initial concentration of PNP in the aqueous solution (100 mL) for the degradation tests was 20 mg L^{-1} under the simulated sun light and 5 mg L^{-1} under the visible light, respectively. The concentration of PNP was determined using a UV 1100 spectrophotometer with the detection wavelength at 318 nm.

Results and discussion

Figure 1a shows the top and cross-sectional (the inset) views of the TiO_2 NTs sample. Clearly, the self-organized TiO_2 nanotubes consist of vertically aligned compact nanotube arrays with a tube diameter of ~90 nm, and length of ~320 nm (the inset). Figures 1b and c display the top and cross-sectional images of the $Zn_{0.5}Mg_{0.5}Fe_2O_4$@TiO_2 NTs sample. The resulting highly ordered and vertically oriented nanotube arrays can be observed from Fig. 1b-c. It is obvious that the deposited nanoparticles not only entered the inner tubes but also surrounded the top of nanotube arrays without blocking the tube entrances. The nanotubes are still open at the top, indicating that the doping process of $Zn_{0.5}Mg_{0.5}Fe_2O_4$ did not destroy the structure of the nanotubes, which would induce the doped species in a much more uniform and compact manner within the inner-surface and outer-surface of the nanotube arrays. From the EDX spectrum of $Zn_{0.5}Mg_{0.5}Fe_2O_4$@TiO_2 NTs (Fig. 1d), it can be noticed that the as-prepared composite nanotube arrays contain Zn, Mg, Fe.

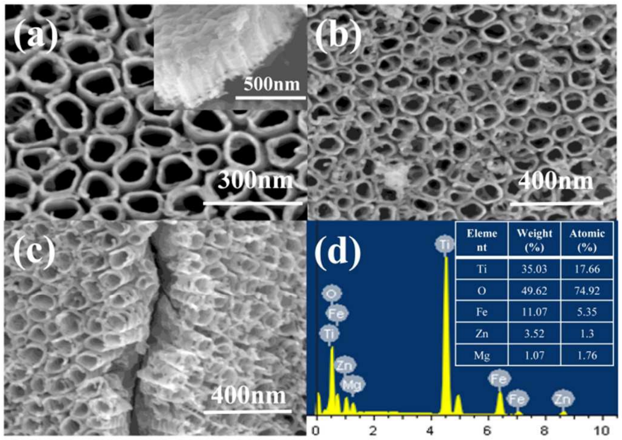

Element	Weight (%)	Atomic (%)
Ti	35.03	17.66
O	49.62	74.92
Fe	11.07	5.35
Zn	3.52	1.3
Mg	1.07	1.76

Fig. 1 Morphologies of TiO_2 nanotube arrays: (a) a typical top-view SEM image of TiO_2 NTs. (inset is the cross-sectional image of TiO_2 NTs); (b) a Top-view SEM image of the $Zn_{0.5}Mg_{0.5}Fe_2O_4$@TiO_2 NTs; (c) a cross-sectional view of $Zn_{0.5}Mg_{0.5}Fe_2O_4$@TiO_2 NTs; (d) EDX of $Zn_{0.5}Mg_{0.5}Fe_2O_4$@TiO_2 NTs (inset table is the weight and atomic percentages of each element).

To further demonstrate the microstructure characteristics of $Zn_{0.5}Mg_{0.5}Fe_2O_4$ nanoparticles deposited on TiO_2 NTAs, the low (Fig. 2a-c) and high magnification (Fig. 2d) TEM images of $Zn_{0.5}Mg_{0.5}Fe_2O_4$/TiO_2 NTAs have been conducted. As exhibited by the low magnification TEM images in Fig. 2a and b, $Zn_{0.5}Mg_{0.5}Fe_2O_4$ nanoparticles are deposited on the tubes entrance while causing no damage of nanotubes. Seen from Fig. 2c, it can be found that $Zn_{0.5}Mg_{0.5}Fe_2O_4$ nanoparticles with a diameter of 20-30 nm are deposited into the tube. Figure 2d depicts the HRTEM image of the selected area, where the lattice fringes of 0.253 nm and 0.351 nm correspond to the reflections from the (311) planes of spinel $Zn_{0.5}Mg_{0.5}Fe_2O_4$ (JCPDS no. 04-002-5442)[34] and the (101) plane of anatase TiO_2 (JCPDS no. 21-1272)[6], respectively. The TEM testing results confirm that spinel ferrite $Zn_{0.5}Mg_{0.5}Fe_2O_4$ nanoparticles are successfully deposited to TiO_2 NTAs.

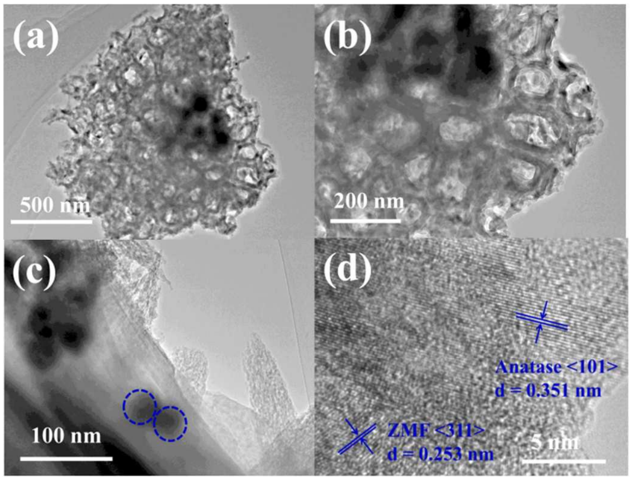

Fig. 2 TEM (a-c) and HRTEM (d) images of the $Zn_{0.5}Mg_{0.5}Fe_2O_4$/TiO_2 NTAs nanocomposite electrode.

In order to identify the crystal phases of TiO_2 NTs and $Zn_{0.5}Mg_{0.5}Fe_2O_4$@TiO_2 NTs, XRD measurements was conducted under specified conditions. Figure 3 shows the XRD patterns of TiO_2 NTs and $Zn_{0.5}Mg_{0.5}Fe_2O_4$@TiO_2 NTs, respectively. The diffraction peaks at 35.2°, 38.4°, 40.3° and 53.1° correspond to (100), (002), (101) and (102) crystal faces of the Ti sheet (JCPDS no. 07-6265). Obviously, TiO_2 NTs annealed at 773K possesses the crystal structure of anatase (2θ = 25.3°, 48.1°. JCPDS no. 07-6175). After the deposition of $Zn_{0.5}Mg_{0.5}Fe_2O_4$, four additional diffraction peaks are identified at 2θ = 30.1°, 35.4°, 43.1° and 57°, which are in accordance with the (220), (331), (400) and (511) planes of spinel $Zn_{0.5}Mg_{0.5}Fe_2O_4$ (JCPDS no. 04-001-9289) respectively [35]. The sharp peak near 35.3° in Fig. 3b is attributed to the overlap and accumulation of 35.2° from anatase and 35.4° from spinel ferrite. It should be noted that isolated MgO, Fe_2O_3 and ZnO phases are not found in the obtained $Zn_{0.5}Mg_{0.5}Fe_2O_4$@TiO_2 NTs sample. The XRD results indicate that the composite nanostructures grown on electrodes prepared by the ultrasonically assisted electrodeposition approach are composed of the desired spinel $Zn_{0.5}Mg_{0.5}Fe_2O_4$ and anatase TiO_2 crystalline structures.

Figure 4a shows the UV-Vis DRS of the TiO_2 NTs and $Zn_{0.5}Mg_{0.5}Fe_2O_4$@TiO_2 NTs. It can be seen that, in the visible light

RSC Advances Accepted Manuscript

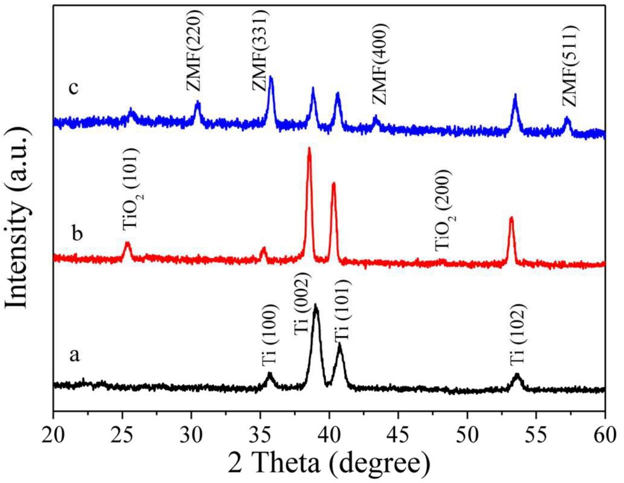

Fig. 3 XRD patterns of Ti sheet (a), TiO_2 nanotube arrays (b), and $Zn_{0.5}Mg_{0.5}Fe_2O_4@TiO_2$ NTs (c), (ZMF in Figure 3 c represents $Zn_{0.5}Mg_{0.5}Fe_2O_4$).

region, the absorption intensity of the sample $Zn_{0.5}Mg_{0.5}Fe_2O_4@TiO_2$ is dramatically increased, which clearly reveals that $Zn_{0.5}Mg_{0.5}Fe_2O_4@TiO_2$ NTs are more sensitive to the visible light than that of the non-doped NTs, therefore, it follows that the $Zn_{0.5}Mg_{0.5}Fe_2O_4@TiO_2$ NTs electrode possesses a much improved photoelectrochemical capability under visible light irradiation. At the same time, an obviously red shift of the absorption threshold toward the visible light region has been successfully observed for the $Zn_{0.5}Mg_{0.5}Fe_2O_4$-doped sample. Two characteristic absorption peaks of TiO_2 at about 410 nm and 540 nm corresponded to the absorption of the trapped hole and the trapped electron, respectively, which result from the sub-bandgap of surface defects on TiO_2 nanotubes. According to literatures[36, 37], the hole traps or deep electron-acceptor type defects showed a peak absorption at around $\lambda = 410$ nm. The electron traps exhibited another peak absorption around $\lambda = 540$ nm, which can be attributed to the oxygen vacancies related sub-bandgap states of the TiO_2 NTs. Figure 4b shows the $(\alpha h\nu)^2$ verse $h\nu$ curve of TiO_2 and $Zn_{0.5}Mg_{0.5}Fe_2O_4@TiO_2$ NTs coming from the equation $(\alpha h\nu)^2 = k(h\nu - E_g)$, where α, h, ν and E_g represent the adsorption coefficient, Planck constant, light frequency and band energy, respectively [38, 39]. For TiO_2 NTs, the absorption onset is at approximately 387 nm, which corresponds well to the band gap 3.18 eV of anatase TiO_2. The absorption of TiO_2 NTs in the visible range could be assigned to the sub-band gap states of the TiO_2 NTs [40]. After the deposition of $Zn_{0.5}Mg_{0.5}Fe_2O_4$ nanoparticles, the absorption threshold shifts to 570 nm. The band gap is estimated to be 2.0 eV.

Consequently, the DRS spectra suggest that the $Zn_{0.5}Mg_{0.5}Fe_2O_4$-doped nanotube arrays might exhibit a higher visible light response than the non-doped NTs. arrays might exhibit a higher visible light response than the non-doped NTs.

In order to reveal the impact of $Zn_{0.5}Mg_{0.5}Fe_2O_4@TiO_2$ NTs photo-induced charge separation, migration and combinations [41], PL spectra of the samples are characterized. Figure 5 presents the TiO_2 NTs and $Zn_{0.5}Mg_{0.5}Fe_2O_4$ @TiO_2 NTs PL spectra. The excitation wavelength of the samples tested was 325 nm. TiO_2 NTs and doped TiO_2 NTs in the vicinity of 400 nm exhibit a strong emission peak.

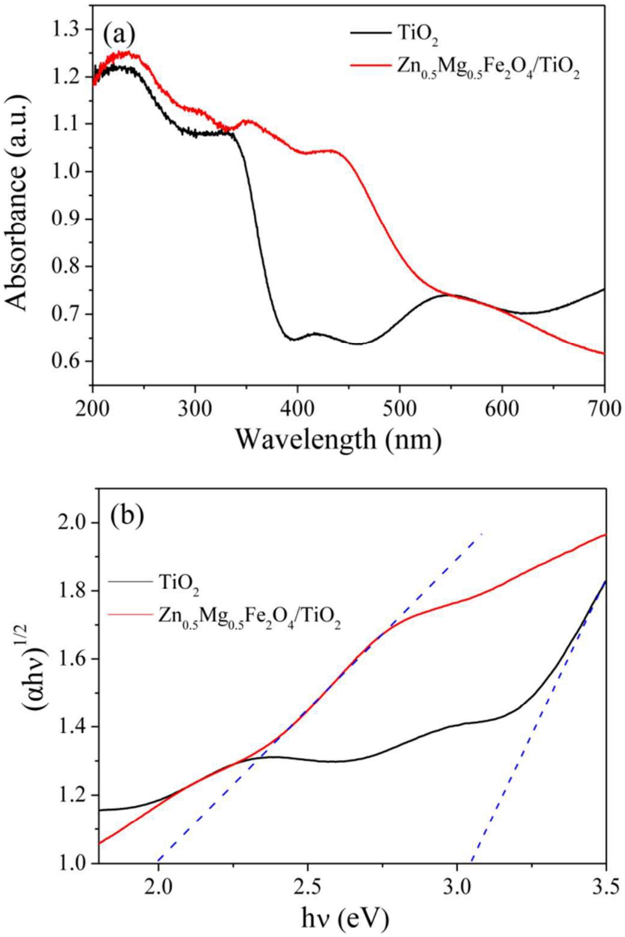

Fig. 4 (a) UV-Vis DRS of TiO_2 NTs and $Zn_{0.5}Mg_{0.5}Fe_2O_4@TiO_2$ NTs; (b) Tauc's plots to determine the band gaps for TiO_2 NTs and $Zn_{0.5}Mg_{0.5}Fe_2O_4@TiO_2$ NTs.

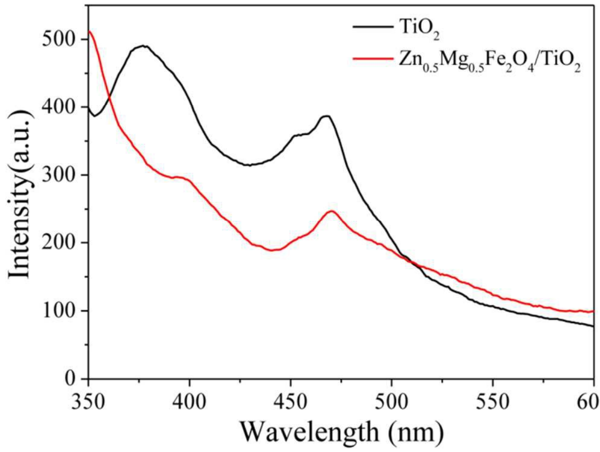

Fig. 5 PL spectra of TiO_2 NTs and $Zn_{0.5}Mg_{0.5}Fe_2O_4@TiO_2$ NTs

Two weak emission peaks also exist around 454 nm and 529 nm, respectively. The emission peak around 400 nm is attributed to the band edge emission of TiO_2 NTs (intrinsic luminescence), corresponding to electron transitions between the emission band [42]. The two weak peeks around 454 nm and 529 nm are ascribed to TiO_2

RSC Advances Accepted Manuscript

NTs with edges of free excitons and bound excitons. These PL signals are mainly due to oxygen vacancies and defects generated on the nanoparticle surface [43, 44]. Compared with the PL spectra of TiO_2 NTs and doped TiO_2 NTs, the PL intensity of $Zn_{0.5}Mg_{0.5}Fe_2O_4$@TiO_2 NTs is found to be significantly reduced. Since the PL spectrum results from the recombination of electrons and holes, a lower luminous intensity means less recombination of electrons and holes. The experimental results clearly indicate that the recombination ratio of photo-generated electron-hole pairs is much lowered due to the loading of $Zn_{0.5}Mg_{0.5}Fe_2O_4$ [45].

To confirm the states of elements and composition information in the nanotubular samples, XPS was employed to reveal the valence states and surface chemical compositions of the composite nanotube arrays. Elements of Ti, Mg, Zn, Fe, O and adventitious carbon are totally proved to be presented in the composite (Fig. 6a). Carbon is ascribed to the adventitious hydrocarbon from the XPS instrument itself. In Fig. 6b, two peaks for the Ti 2p are observed at binding energy 464.8 eV and 459.2 eV, which are assigned to Ti $2p_{1/2}$ and Ti $2p_{3/2}$ respectively. These values are in good agreement with the XPS data known for Ti^{4+} in the pure anatase titania form [46] in the corresponding literature. It seems that loading $Zn_{0.5}Mg_{0.5}Fe_2O_4$ species did not have any effect on the position of Ti 2p peak. As shown in Fig. 6c, XPS peaks of Zn 2p located at 1044.4 eV and 1022.8 eV can be assigned to the spectra of Zn $2p_{1/2}$ and Zn $2p_{3/2}$, suggesting that the composite electrode contains Zn^{2+} [47]. In Fig. 6d, the peaks located at 710.6 eV and 724.4 eV can be attributed to Fe $2p_{3/2}$ and Fe $2p_{1/2}$ for Fe^{3+}, respectively, which reveal the oxidation state of Fe^{3+} in the nanocomposites [48]. In addition, in Fig. 6e, it can be found that a sharp peak around 1303.8 eV, which matches well with Mg 1s, indicating that Mg exists in Mg^{2+} oxidation state in the composite electrode [33]. As shown in Fig. 6f, O 1s peak is asymmetric suggesting at least two kinds of oxygen species are present in and near the surface region. Meanwhile, the XPS spectra of O 1s of the $Zn_{0.5}Mg_{0.5}Fe_2O_4$@TiO_2 NTs are fitted using Gaussian – Lorentzian peak shapes, which can be devolved into three small peaks. The peak located at 532.4 eV is assigned to the adsorbed oxygen. The other two peaks located at 529.4 eV and 530.1 eV are attributed to the O element in TiO_2 and $Zn_{0.5}Mg_{0.5}Fe_2O_4$, respectively [49].

To further demonstrate the effect of $Zn_{0.5}Mg_{0.5}Fe_2O_4$ on expanding the active spectral range of doped TiO_2 NTs, SPV characterization of the as-prepared electrodes was conducted (Fig.7). TiO_2 NTs electrode presents a response in the UV range from 300 to 380 nm, which is ascribed to the electron transition from valence band to conduction band of TiO_2 ($O_{2p}\rightarrow Ti_{3d}$) [50]. However, the $Zn_{0.5}Mg_{0.5}Fe_2O_4$@TiO_2 NTs electrode displays a stronger SPV signal than that of the TiO_2 NTs electrode. The modified electrode exhibits a red shift of the spectral band towards visible region, which is also confirmed by the UV-Vis DRS characterization. In view of that the strong SPV signal has direct correlation with effective separation of photo-generated charge carriers [51], the presence of $Zn_{0.5}Mg_{0.5}Fe_2O_4$ would favor the photo-induced charge carrier separation and surface-interface transfer, greatly enhancing the PC and PEC activity of TiO_2 NTs electrode.

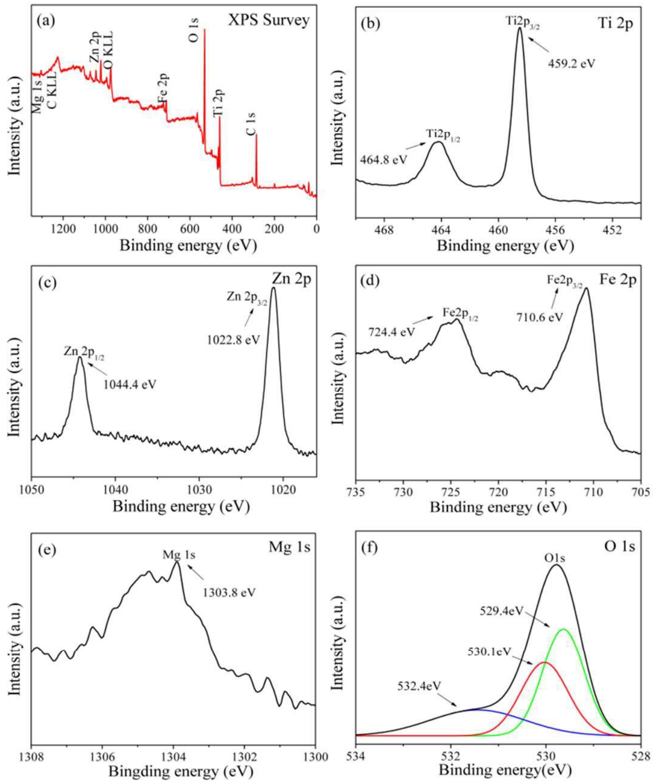

Fig. 6 The whole XPS (a), Ti 2p (b), Fe 2p (c), Zn 2p (d), Mg 1s (e) and O 1s (f) XPS of $Zn_{0.5}Mg_{0.5}Fe_2O_4$@TiO_2 composite NTs.

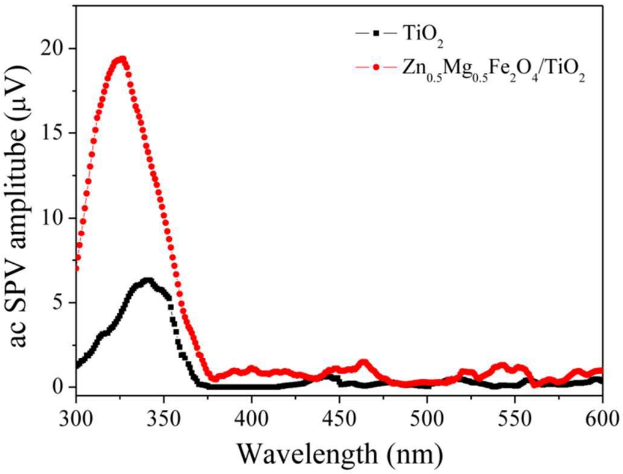

Fig. 7 SPV spectra of the as-prepared TiO_2 NTs and $Zn_{0.5}Mg_{0.5}Fe_2O_4$@TiO_2 NTs samples.

Photoelectrochemical Performance

The Photoelectrochemical performance of TiO_2 NTs and $Zn_{0.5}Mg_{0.5}Fe_2O_4$@TiO_2 NTs was investigated under visible light and simulated sun light irradiation. The photocurrent densities as a function of the applied potential of the electrodes in a 0.01M Na_2SO_4 solution are presented in Figs.8a and c. The dark current densities

RSC Advances Accepted Manuscript

are low and negligible under visible light and simulated sun light irradiation. However, TiO_2 still displays a noticeable response while the photocurrent density of doped TiO_2 NTs dramatically rises under the visible light. The increase and subsequent decrease of photocurrent density is believed to be due to the fact that the space charge region of the heterojunction promotes the separation of photo-induced carriers by the internal electrostatic field in the heterojunction region. As a consequence, more charge carriers would participate in reactions instead of recombination [52]. However, this internal electrostatic field of the junction region would be weakened with increasing the applied bias potential because the thickness of the space charge layer decreased with the bias voltage. As a result, less charge carriers could be separated, and the photocurrent density decreases accordingly [53, 54]. The saturated photocurrent density of the $Zn_{0.5}Mg_{0.5}Fe_2O_4$@TiO_2 NTs electrode, at 0.13 mA cm^{-2} is about 6.5 folds as high as that of TiO_2 NTs at 0.02 mA cm^{-2} under visible light irradiation. In the meantime, the photocurrent density of the doped TiO_2 NTs electrode is more than 4 folds as high as that of the TiO_2 NTs (1.75 versus 0.4 mA cm^{-2}) under simulated sun light irradiation. It may therefore be concluded that $Zn_{0.5}Mg_{0.5}Fe_2O_4$@TiO_2 NTs has a much higher conversion capability of visible light than TiO_2 NTs, at a 10 folds increase, and the photo-generated carrier-separation efficiency has been improved significantly after being modified with $Zn_{0.5}Mg_{0.5}Fe_2O_4$ nanoparticles. As shown in Fig. 8b and d, after loading $Zn_{0.5}Mg_{0.5}Fe_2O_4$ nanoparticles, the photo-conversion efficiency has been improved under simulated sun light and visible light irradiation. The photo-conversion efficiency (η) of light energy to chemical energy in the presence of a bias potential is calculated as follows [6].

$$\eta(\%) = \frac{\text{total power output - electrical power input}}{\text{light power input}} \times 100$$

$$= [j_p\ (E_{rev}{}^{0} - |E_{app}|)\ \times 100] / I_0$$

Where, j_p means the photocurrent density (mA cm^{-2}), $j_p E_{rev}{}^{o}$ is the total power output; $j_p|E_{app}|$ represents the electrical power input; and I_o is the power density of the incident light (mA cm^{-2}). $E_{rev}{}^{o}$ is the standard reversible potential (which is 1.23 V for the water-splitting reaction when pH value reaches 0), and $|E_{app}|$ is the absolute value of the applied potential E_{app}, which can be calculated as $E_{app} = E_{meas} - E_{aoc}$, where E_{meas} is the electrode potential (vs SCE) of the working electrode at which the photocurrent is measured under illumination and E_{aoc} is the electrode potential (vs SCE) of the same working electrode under open-circuit conditions, under the same condition.

In order to study the properties of the electrodes and their interactions with the solution, the EIS measurements of the TiO_2 NTs and $Zn_{0.5}Mg_{0.5}Fe_2O_4$@TiO_2 NTs are carried out, which cover the frequencies of 10^5 to 10^{-2} Hz intervals by an amplitude of 10 mV at an open circuit potential under dark and visible light irradiation [49]. By controlling the electrode current or potential, the EIS curves of the as-prepared electrode vary by slight amplitude sinusoidal curve with time, while measuring the potential or current variation with time of the electrode [55]. Figure 9 exhibits the EIS results of the TiO_2 NTs and $Zn_{0.5}Mg_{0.5}Fe_2O_4$@TiO_2 NTs electrodes under dark and visible illumination in the 0.01 M Na_2SO_4 electrolyte, with the bias voltage set to 0.3 V. The results in Fig. 9 suggest that without any light irradiation, the Nernst curve of TiO_2 NTs becomes close to a straight line, indicating that the TiO_2 NTs electrode response is poor without any light irradiation. The impedance of the radius of the TiO_2 NTs electrode decreases sharply after $Zn_{0.5}Mg_{0.5}Fe_2O_4$ loading or with visible light irradiation, which means that the composite material has a good response to visible light region. The EIS measurement results illustrate that $Zn_{0.5}Mg_{0.5}Fe_2O_4$ loading effectively improves the separation of photon-generated electron-hole pairs and accelerates the photon-generated charge transfer between $Zn_{0.5}Mg_{0.5}Fe_2O_4$ and TiO_2 NTs interface. It is concluded that the doping $Zn_{0.5}Mg_{0.5}Fe_2O_4$ nanoparticles effectively accelerate the transfer of photon-generated charge carriers.

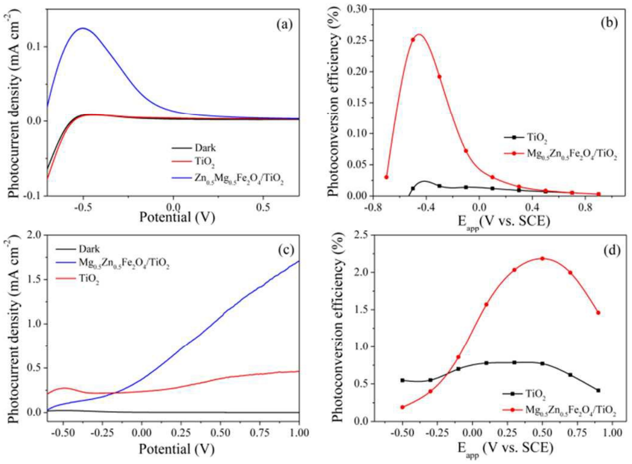

Fig. 8 I-V characteristics of TiO_2 and $Zn_{0.5}Mg_{0.5}Fe_2O_4$@TiO_2 NTs under visible light (I_o = 33.5 mW cm^{-2}, $\lambda > 420$ nm, 0.6 V vs. SCE in 0.01 M Na_2SO_4) and simulated sun light irradiation (I_o = 36 mW cm^{-2}, 0.6 V vs. SCE in 0.01 M Na_2SO_4) (a) and, (c); and photoconversion efficiency as a function of applied bias potential under visible light and simulated sun light irradiation (b), and (d).

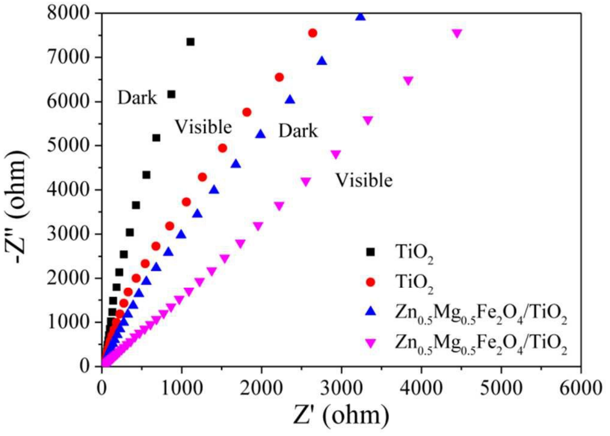

Fig. 9 EIS Nynquist plots of TiO_2 NTs electrode and $Zn_{0.5}Mg_{0.5}Fe_2O_4$@TiO_2 NTs electrode under dark and visible light irradiation ($\lambda > 420$ nm, I_o = 33.5 mW cm^{-2}) (The bias potential is 0.3 V (vs. SCE) in a 0.01 M Na_2SO_4 aqueous solution).

RSC Advances Accepted Manuscript

RSC Advances Accepted Manuscript

Degradation of PNP

To evaluate the PEC activity of the $Zn_{0.5}Mg_{0.5}Fe_2O_4$@TiO_2 NTs electrode, a series of experiments for PNP degradation were carried out. After irradiation for 120 min under simulated sun light, the concentration of PNP was almost unchanged in the direct photocatalytic (DP) degradation without any photocatalyst, while 10.5% of PNP was degraded in the electrochemical process (EC) (Fig. 10a). The degradation efficiency of PNP by PC degradation was 36% with the $Zn_{0.5}Mg_{0.5}Fe_2O_4$@TiO_2 composite nanotube array electrode. When a bias potential of 0.6 V (vs. SCE) was applied, the degradation efficiency increased to about 69% for the $Zn_{0.5}Mg_{0.5}Fe_2O_4$ loaded electrode, an enhanced of PNP than heterojunction network catalyst of Cu_2O/TiO_2 [56]. Compared with the non-doped TiO_2 NTs, the composite electrodes afford a 2 folds increase in the efficiency in PNP degradation. In the meantime,trends can be observed in Fig. 10c, where the EC, DP, PC and PEC degradation efficiency of PNP by $Zn_{0.5}Mg_{0.5}Fe_2O_4$ are 9.3% 10.3% 14.8% and 59%, respectively, when illuminated by visible light while the PEC degradation of PNP is just 21% by TiO_2 NTs alone. Judging from the increased degradation efficiency, there exists an obvious synergistic effect between the EC process and the PC process (under both simulated sun light irradiation and visible light irradiation, respectively). The enhanced PEC activity of the composite electrode could be attributed to the comprehensive effect between the lowered electron-hole recombination rate by the applied bias potential and the wider spectral response promoted by the $Zn_{0.5}Mg_{0.5}Fe_2O_4$ nanoparticles [6, 56]. Thus the applied bias potential effectively inhibits the recombination of photo-generated electron-hole pairs and prolongs the life of the photo-generated charge carriers, hence yielding a better photoelectrochemical performance. As shown in Fig. 10b and d, the kinetics of PNP degradation processes in EP, DP, PC, and PEC by $Zn_{0.5}Mg_{0.5}Fe_2O_4$ doped electrode and PEC by TiO_2 NTs follows a pseudo-first-order kinetics, as described in Table 1.

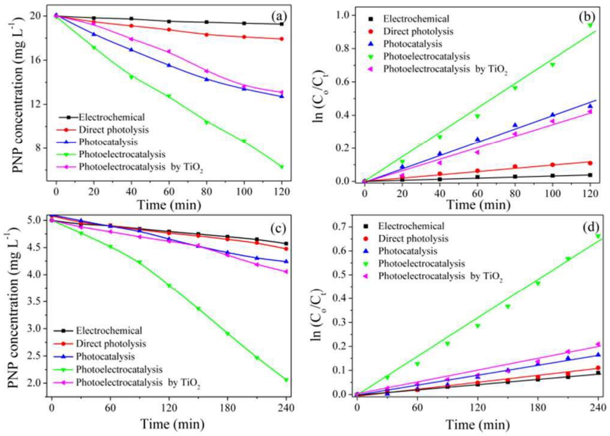

Fig. 10 The PNP concentration vs. time plots in the PNP degradation tests with nanocomposite electrodes in different processes under simulated sun light irradiation: (a) (I_o = 36 mW cm^{-2}, 0.6 V vs. SCE, C_o = 20 mg L^{-1}) and visible light irradiation (c) (I_o = 33.5 mW cm^{-2}, λ > 420 nm, 0.6 V vs. SCE, C_o = 5 mg L^{-1}); and kinetic constants and regression coefficients of degradation for PNP obtained under simulated sun light irradiation (b) and visible light irradiation (d).

Table 1 Kinetic constants and regression coefficients for PNP degradation using different processes under simulated sun light (a) and visible light irradiation (b).

(a)	Processes	Kinetic constants (min^{-1})	R^2
	EC	3×10^{-4}	0.9441
	DP	9×10^{-4}	0.9794
	PC	3.7×10^{-3}	0.9912
	PEC	8×10^{-3}	0.9906
	TiO_2	3.8×10^{-3}	0.9872

(b)	Processes	Kinetic constants (min^{-1})	R^2
	EC	4×10^{-5}	0.9873
	DP	5×10^{-5}	0.9882
	PC	8×10^{-4}	0.9933
	PEC	2.8×10^{-3}	0.9941
	TiO_2	8×10^{-4}	0.9713

To further investigate the active species involved in PEC degradation, we have conducted the capture of the active species in PNP degradation to determine which species play a major role in PNP degradation. As exhibited in Fig. 11, the PEC degradation of PNP was inhibited to some extent by the addition of t-BuOH (hydroxyl radicals scavenger) under simulated sun light irradiation, indicating that the hydroxyl radicals were confirmed as active oxidative species in the PEC process. However, it was intensively suppressed when EDTA (holes scavenger) was introduced. This result indicates that photogenerated holes were the main active oxidizing species involved in the PEC process compared with other species. The direct holes transfer mainly governed the PC process. Meanwhile, $\bullet O_2^-$ might also serve as active species in this reaction. N_2 was used to confirm the effect of O_2 and the results are shown in Fig. 11. Under the anoxic condition, the degradation of PNP was not completely inhibited, indicating that $\bullet O_2^-$ was active species but not the main one. In summary, the photogenerated holes account for the photo activity most compared with •OH and $\bullet O_2^-$ in PEC degradation of PNP.

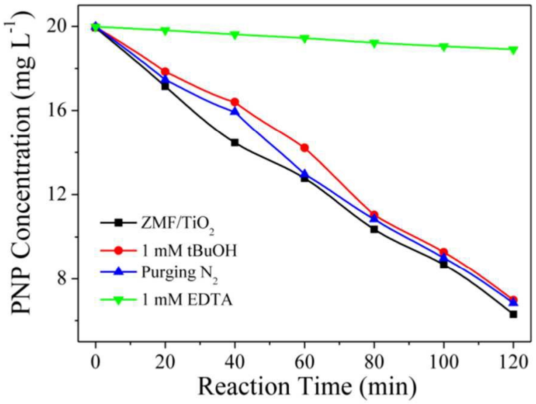

Fig. 11 Plots of photogenerated active species trapped in the system of photodegradation of PNP by $Zn_{0.5}Mg_{0.5}Fe_2O_4/TiO_2$ NTAs under simulated light irradiation (I_o = 36 mW cm^{-2}, 0.6 V vs. SCE and C_o = 20 mg L^{-1} in 0.01M Na_2SO_4).

The stability and recyclability of the as-prepared electrode was evaluated by repeating the PNP degradation under simulated sun light irradiation several times. Before each repeating experiment, the composite electrode was ultrasonically cleaned with deionized water and each new PEC degradation cycle was carried out by introducing a fresh PNP solution and Na_2SO_4 electrolyte under the same conditions. As shown in Fig. 12, the efficiency of PNP degradation shows no obvious decline in the PEC activity of $Zn_{0.5}Mg_{0.5}Fe_2O_4$@TiO_2 NTs after five recycles. Therefore, it is reasonably concluded that the $Zn_{0.5}Mg_{0.5}Fe_2O_4$@TiO_2 NTs electrode exhibits fair stability and can be optimized as a suitable candidate for PEC purification of PNP polluted water.

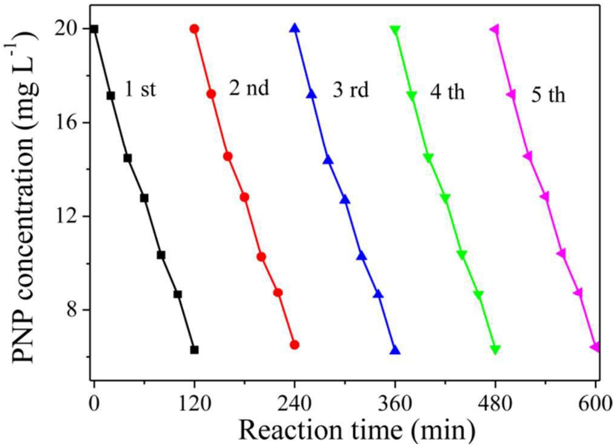

Fig. 12 PEC degradation of PNP by the $Zn_{0.5}Mg_{0.5}Fe_2O_4$@TiO_2 NTs electrode over five consecutive cycles under simulated sun light illumination.

Mechanism of Enhanced PEC Activity

To gain a further insight into the enhanced PEC activity, the charge transfer behavior during PNP degradation is illustrated in Fig. 13. The involved photoelectrocatalytic reactions of PNP degradation over $Zn_{0.5}Mg_{0.5}Fe_2O_4$@TiO_2 nanotube arrays have been described as follows (herein, ZMF represents $Zn_{0.5}Mg_{0.5}Fe_2O_4$). To calculate the band structures of $Zn_{0.5}Mg_{0.5}Fe_2O_4$, periodic density functional calculations (DFT) computations were performed using a plane-wave method implemented in the Cambridge Sequential Total Energy Package (CASTEP) code[57, 58]. It can be obtained that the band gap of $Zn_{0.5}Mg_{0.5}Fe_2O_4$ is approximately 1.9 eV, in good agreement with DRS experimental values 2.0 eV. (the conduction band and valence band structure of $Zn_{0.5}Mg_{0.5}Fe_2O_4$ can be seen in electronic supplementary information). As shown in Fig. 13, under visible light irradiation, $Zn_{0.5}Mg_{0.5}Fe_2O_4$ with a narrow band gap can be easily excited to generate electron-hole pairs while TiO_2 with a band gap of 3.2 eV can not be excited. The photo-generated electrons can be forced to transfer from the conduction band of $Zn_{0.5}Mg_{0.5}Fe_2O_4$ to TiO_2 under an applied bias potential of 0.6 V, leaving more holes in the valence band of $Zn_{0.5}Mg_{0.5}Fe_2O_4$, significantly reducing the charge recombination. However, the holes spontaneously transfer from TiO_2 NTs to the valence band of $Zn_{0.5}Mg_{0.5}Fe_2O_4$ nanoparticle. This separation effectively prevent the $Zn_{0.5}Mg_{0.5}Fe_2O_4$ react with H_2O or hydroxyl ions (OH^-) to form

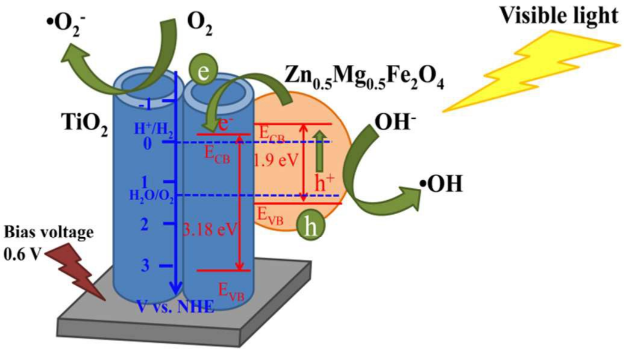

Fig. 13 Schematic illustration of the mechanism of photocatalytic degradation of PNP using $Zn_{0.5}Mg_{0.5}Fe_2O_4$@TiO_2 NTs as the photocatalyst under visible light irradiation ($\lambda > 420$ nm, $I_o = 33.5$ mW cm^{-2}).

$$\text{ZMF} + \text{Visible light} \rightarrow \text{ZMF}(h^+) + \text{ZMF}(e^-)$$
$$\text{ZMF}(e^-) + TiO_2 \rightarrow \text{ZMF} + TiO_2(e^-)$$
$$TiO_2(e^-) + O_2 \rightarrow TiO_2 + \bullet O_2^-$$
$$\bullet O_2^- + H^+ \rightarrow \bullet OOH \rightarrow H_2O_2$$
$$H_2O_2 + \bullet O_2^- \rightarrow \bullet OH + OH^-$$
$$TiO_2(e^-) + \text{external electrostatic field} \rightarrow \text{external circuit}$$
$$\rightarrow \text{Counter electrode}$$
$$\text{ZMF}(h^+) + OH^- \rightarrow \text{ZMF} + \bullet OH$$
$$\text{PNP} + \bullet OH,\ \bullet O_2^-,\ h^+ \rightarrow \text{Intermediate} + H_2O + CO_2$$

hydroxyl radicals (•OH). The accumulated electrons in the conduction band of TiO_2 are transferred to the adsorbed O_2 on the TiO_2 surface to form superoxide radical anions ($\bullet O_2^-$), which are then reduced to •OH. Eventually, the photo-generated active oxidizing species such as •OH, $\bullet O_2^-$ and h^+ are involved in the self-sensitized photoelectrocatalysis degradation of PNP.

Conclusions

A novel $Zn_{0.5}Mg_{0.5}Fe_2O_4$@TiO_2 composite-nanotube-array photo-electrode was successfully synthesized using an ultrasonically assisted electrodeposition technique. The electrodeposition strategy effectively promoted the deposition of the $Zn_{0.5}Mg_{0.5}Fe_2O_4$ nanoparticles within self-organized and vertically oriented TiO_2 nanotube arrays while minimizing the clogging of the nanotube entrances. The PEC properties demonstrated that the composite nanotube arrays showed typical heterojunction characteristics. The loading of $Zn_{0.5}Mg_{0.5}Fe_2O_4$ nanoparticles significantly extended the response of the TiO_2 nanotube arrays to the visible light region. The composite nanotube arrays showed a significantly higher photocurrent density and improved photo-conversion efficiency due to better charge separation and collection efficiency under simulated sun light and visible light illumination. In addition, the composite electrode was found to possess excellent PEC activity for the degradation of PNP as compared with the non-doped TiO_2 electrode under both simulated sun light and visible light illumination. Consequently, the $Zn_{0.5}Mg_{0.5}Fe_2O_4$@TiO_2 heterostructure photoelectrode described herein may be used in a wide range of

RSC Advances Accepted Manuscript

applications including photocatalysis.

Acknowledgements

This work received partial financial support from the National Nature Science Foundation of China (No NSFC21377015, 21207015), the Major State Basic Research Development Program of China (973 Program) (No. 2011CB936002) and the Key Laboratory of Industrial Ecology and Environmental Engineering, China Ministry of Education.

Notes and references

1. X. Chen, S. Shen, L. Guo and S. S. Mao, *Chem. Rev.*, 2010, **110**, 6503-6570.
2. H. Kisch, *Angew. Chem. Int Ed.*, 2013, **52**, 812-847.
3. A. L. Linsebigler, G. Lu and J. T. Yates Jr, *Chem. Rev.*, 1995, **95**, 735-758.
4. S. G. Kumar and L. G. Devi, *J. Phys. Chem. A*, 2011, **115**, 13211-13241.
5. K. Lee, D. Kim, P. Roy, I. Paramasivam, B. I. Birajdar, E. Spiecker and P. Schmuki, *J. Am. Chem. Soc.*, 2010, **132**, 1478-1479.
6. A. Zhu, Q. Zhao, X. Li and Y. Shi, *ACS Appl. Mate. Interfaces*, 2014, **6**, 671-679.
7. T. Li, X. Li, Q. Zhao, Y. Shi and W. Teng, *Appl. Catal. B: Enviro.*, 2014, 156-157, 362-370.
8. A. E. R. Mohamed and S. Rohani, *Energy Environ. Sci.*, 2011, **4**, 1065-1086.
9. R. M. Navarro, M. C. Alvarez-Galván, J. A. V. de la Mano, S. M. Al-Zahrani and J. L. G. Fierro, *Energy Environ. Sci.*, 2010, **3**, 1865-1882.
10. C. X. Kronawitter, L. Vayssieres, S. Shen, L. Guo, D. A. Wheeler, J. Z. Zhang, B. R. Antoun and S. S. Mao, *Energy Environ. Sci.*, 2011, **4**, 3889-3899.
11. A. Lamberti, A. Sacco, S. Bianco, D. Manfredi, F. Cappelluti, S. Hernandez, M. Quaglio and C. F. Pirri, *Phys. Chem. Chem. Phys.* 2013, **15**, 2596-2602.
12. L. Xue, Z. Wei, R. Li, J. Liu, T. Huang and A. Yu, *J..Mater. Chem.*, 2011, **21**, 3216-3220.
13. L. Sun, S. Zhang, X. W. Sun, X. Wang and Y. Cai, *Langmuir*, 2010, **26**, 18424-18429.
14. W. Teng, X. Y. Li, Q. D. Zhao and G. H. Chen, *J. Mater. Chem. A*, 2013, **1**, 9060-9068.
15. W. Wang, M. Tian, A. Abdulagatov, S. M. George, Y. C. Lee and R. Yang, *Nano Lett.*, 2012, **12**, 655-660.
16. J. Choi, H. Park and M. R. Hoffmann, *J. Phys. Chem. C*, 2009, **114**, 783-792.
17. M. A. Hashemian, E. Palacios, I. I. Nedrygailov, D. Diesing and E. Karpov, *ACS Appl. Mater. Interfaces*, 2013, **5**, 12375-12379.
18. W. Tu, Y. Zhou, Q. Liu, S. Yan, S. Bao, X. Wang, M. Xiao and Z. Zou, *Adv. Funct. Mater.*, 2013, **23**, 1743-1749.
19. H. U. Lee, S. C. Lee, S. H. Choi, B. Son, S. J. Lee, H. J. Kim and J. Lee, *Appl. Catal. B: Environ.*, 2013, **129**, 106-113.
20. A. Ghicov, J. M. Macak, H. Tsuchiya, J. Kunze, V. Haeublein, L. Frey and P. Schmuki, *Nano Lett.*, 2006, **6**, 1080-1082.
21. M. Wang, L. Sun, Z. Lin, J. Cai, K. Xie and C. Lin, *Energy Environ. Sci.* 2013, **6**, 1211.
22. G. Li, L. Wu, F. Li, P. Xu, D. Zhang and H. Li, *Nanoscale*, 2013, **5**, 2118-2125.
23. A. Kongkanand, K. Tvrdy, K. Takechi, M. Kuno and P. V. Kamat, *J. Am. Chem. Soc.* 2008, **130**, 4007-4015.
24. Q. Kang, S. Liu, L. Yang, Q. Cai and C. A. Grimes, *ACS Appl. Mater. Interfaces*, 2011, **3**, 746-749.
25. W.-T. Sun, Y. Yu, H.-Y. Pan, X.-F. Gao, Q. Chen and L.-M. Peng, *J. Am. Chem. Soc.*, 2008, **130**, 1124-1125.
26. K. Thummer, M. Chhantbar, K. Modi, G. Baldha and H. Joshi, *J. Magn. Magn. Mater.*, 2004, **280**, 23-30.
27. E. Casbeer, V. K. Sharma and X.-Z. Li, *Sep. Purif. Technol.*, 2012, **87**, 1-14.
28. R. Dom, R. Subasri, K. Radha and P. H. Borse, *Solid State Commun.*, 2011, **151**, 470-473.
29. M. Gaudon, N. Pailhé, A. Wattiaux and A. Demourgues, *Mater. Res. Bull.*, 2009, **44**, 479-484.
30. K. A. Mohammed, A. D. Al-Rawas, A. M. Gismelseed, A. Sellai, H. M. Widatallah, A. Yousif, M. E. Elzain and M. Shongwe, *Phys. B*, 2012, **407**, 795-804.
31. A. Xia, S. Liu, C. Jin, L. Chen and Y. Lv, *Mater. Lett.* 2013, **105**, 199-201.
32. S. Rahman, K. Nadeem, M. Anis-ur-Rehman, M. Mumtaz, S. Naeem and I. Letofsky-Papst, *Ceram. Int.* 2013, **39**, 5235-5239.
33. Y. Hou, F. Zuo, A. Dagg and P. Feng, *Angew. Chem.*, 2013, **52**, 1248-1252.
34. K. Mukherjee and S. Majumder, *Nanotechnol.*, 2010, **21**, 255504.
35. K. Mukherjee and S. Majumder, *Sensors and Actuators B: Chemical*, 2013, **177**, 55-63.
36. Z. Wu, Y. Wang, L. Sun, Y. Mao, M. Wang and C. Lin, *J. Mater. Chem. A,* 2014, **2**, 8223-8229.
37. S. Kurian, H. Seo and H. Jeon, *J. Phys. Chem. C*, 2013, **117**, 16811-16819.
38. M. Paulose, K. Shankar, S. Yoriya, H. E. Prakasam, O. K. Varghese, G. K. Mor, T. A. Latempa, A. Fitzgerald and C. A. Grimes, *J. Phys. Chem. B*, 2006, **110**, 16179-16184.
39. K. Shankar, G. K. Mor, A. Fitzgerald and C. A. Grimes, *J. Phys. Chem. C*, 2007, **111**, 21-26.
40. H. E. Prakasam, K. Shankar, M. Paulose, O. K. Varghese and C. A. Grimes, *J. Phys. Chem. C*, 2007, **111**, 7235-7241.
41. N. Serpone, D. Lawless and R. Khairutdinov, *J. Phys. Chem.*, 1995, **99**, 16646-16654.
42. V. Salas, E. Olias, A. Barrado and A. Lazaro, *Sol. Energy Mater. Sol. Cells*, 2006, **90**, 1555-1578.
43. Y. Lei, L.-D. Zhang, G.-W. Meng, G.-H. Li, X. Zhang, C. Liang, W. Chen and S. Wang, *Appl. Phy. Lett.* 2001, **78**, 1125-1127.
44. T. Tachikawa and T. Majima, *Langmuir* 2009, **25**, 7791-7802.

45 T. Tachikawa, N. Wang, S. Yamashita, S. C. Cui and T. Majima, *Angew. Chem. Int. Ed.*, 2010, **49**, 8593-8597.

RSC Advances Accepted Manuscript

Please do not adjust margins

46. Y. Hou, X.-Y. Li, Q.-D. Zhao, X. Quan and G.-H. Chen, *Adv. Funct. Mate.*, 2010, **20**, 2165-2174.
47. Y.-Q. Chu, Z.-W. Fu and Q.-Z. Qin, *Electrochim. Acta*, 2004, **49**, 4915-4921.
48. Y. Sharma, N. Sharma, G. Rao and B. Chowdari, *Electrochim. Acta*, 2008, **53**, 2380-2385.
49. M. Wang, L. Sun, J. Cai, P. Huang, Y. Su and C. Lin, *J. Mater. Chem. A*, 2013, **1**, 12082.
50. Y. Mizukoshi, N. Ohtsu, S. Semboshi and N. Masahashi, *Appl. Catal. B: Environ.*, 2009, **91**, 152-156.
51. Q. Li and J. K. Shang, *Environ. Sci. Technol.*, 2009, **43**, 8923-8929.
52. Y. Chen, J. C. Crittenden, S. Hackney, L. Sutter and D. W. Hand, *Environ. Sci. Technol.*, 2005, **39**, 1201-1208.
53. Y. Hou, F. Zuo, A. Dagg and P. Feng, *Nano Lett.*, 2012, **12**, 6464-6473.
54. H. Yu, X. Quan, S. Chen and H. Zhao, *J. Phys. Chem. C*, 2007, **111**, 12987-12991.
55. X. Zhao, T. Xu, W. Yao, C. Zhang and Y. Zhu, *Appli. Catal. B: Environ.*, 2007, **72**, 92-97.
56. L. Yang, S. Luo, Y. Li, Y. Xiao, Q. Kang and Q. Cai, *Environ. Sci.. Technol.*, 2010, **44**, 7641-7646.
57. L. Sun, L. Xiang, X. Zhao, C.-J. Jia, J. Yang, Z. Jin, X. Cheng and W. Fan, ACS Catalysis, 2015, **5**, 3540-3551.
58. M. Nolan, ACS applied materials & interfaces, 2012, **4**, 5863-5871.

RSC Advances Accepted Manuscript

This journal is © The Royal Society of Chemistry 20xx